Chemical Science

EDGE ARTICLE

Check for updates

Enhanced reactivity at the oil–water interface accelerates the synthesis of zymonic acid in microemulsions†

Brandon J. Wallace, [ab] Musarrat Makhnun,[cd] Rana Bachnak,[cd] Pyeongeun Kim, [b] Musahid Ahmed, [b] Cari S. Dutcher, [cd] Kevin R. Wilson [*b] and Ashok Ajoy*[ab]

Chemical reactions in microscale compartments, such as aerosols and emulsions, can exhibit significantly faster reaction rates relative to macroscale containers. This enhancement in chemistry is often due to the elevated importance of surfaces as reaction vessels are reduced to picoliter volumes. While most studies have focused on the air–water interface of droplets, there are comparably fewer studies of reactions in micron-scale aqueous solutions encapsulated by oil. Here we investigate the condensation reaction of pyruvic acid (PA) to form zymonic acid (ZA) and water. Using microfluidics and optical trapping, chemical kinetics are measured in monodisperse micron-sized emulsion droplets *in situ via* Raman spectroscopy. Relative to a macroscopic bulk solution, which exhibits little to no reaction over many days, we find efficient production of ZA over the same time period. A kinetic model is developed to elucidate the role of the interface in accelerating the microdroplet reaction kinetics. After quantifying the surface partitioning of PA from interfacial tension measurements, the rate coefficient for the condensation reaction at the oil–water interface is determined to be 1.8×10^{-2} M^{-1} s^{-1}. This rate coefficient is estimated to be 10^5 larger than the reaction rate in bulk aqueous solutions. Compared to previous studies of accelerated ZA formation at the air–water interface on nanodroplets, we find that the reaction at the oil–water interface is 20 times more efficient. Despite this difference, the overall ZA formation rate in emulsions is significantly slower than in the same-sized aerosols, which arises from the weaker partitioning of PA to the oil–aqueous relative to air–water interface. These results highlight the interplay between interfacial partitioning and reactivity in accelerating chemistry in microcompartments and provides new insights into how interfacial composition influences condensation reactions.

I. Introduction

Chemistry occurring within nanometer and micrometer-sized volumes, including emulsions and aerosols, has garnered immense interest due to their ability to enhance reactions relative to beaker-scale reactors.[1–7] While the exact mechanism(s) responsible for this enhancement remains subject to some debate, it is well-established that the prominence of the interface in high surface-area-to-volume microcompartments must play a critical role in accelerating chemical kinetics.[8–10] Reaction rate enhancement arises both from favorable reactant partitioning to the interface and the partially solvated interfacial environment that can lower reaction barriers.[11–13] Of the many reactions purported to be accelerated in microcompartments, condensation reactions, important synthetic routes for building molecular complexity, appear to be a particularly favorable class of reactions for acceleration at interfaces, in electrospray droplets, Leidenfrost droplets, aerosols, emulsions, and thin films.[1,6,7,14–19] Although condensation reactions eliminate water as a product and are generally unfavorable in bulk aqueous solutions, there is evidence that partial solvation at an interface may be sufficient to overcome this substantial thermodynamic barrier.[20]

Most studies on enhanced interfacial chemistry have focused on the air–water interface. However, oil–aqueous interfaces are ubiquitous in nature and include biological cells, emulsions, and the sea-surface microlayer.[21–24] Despite their importance, oil–water interfaces remain comparatively understudied. The use of microfluidics and emulsions also offers several technological advantages, including high throughput generation of emulsion droplets with tunable and reproducible size, long-term stability over days to several weeks, and precise

a Department of Chemistry, University of California, Berkeley, Berkeley, CA 94720, USA. E-mail: ashokaj@berkeley.edu

b Chemical Sciences Division, Lawrence Berkeley National Laboratory, Berkeley, California 94720, USA. E-mail: krwilson@lbl.gov
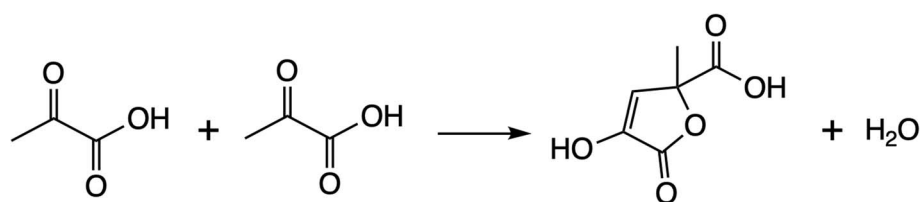
c Department of Mechanical Engineering, University of Minnesota, Minneapolis, MN 55455, USA

d Department of Chemical Engineering and Materials Science, University of Minnesota, Minneapolis, MN 55455, USA

† Electronic supplementary information (ESI) available. See DOI: https://doi.org/10.1039/d5sc03258j

control of interfacial composition and reaction conditions.[25–27] These features enable the study of interfacial processes while offering a scalable platform for interfacial synthesis and material production. To date, there are a few reports of enhanced condensation reactions at the oil–water interface of emulsions and coacervates.[1,12,28] Recently, Krushinski et al.[29] compared the reactivity of enzymes within emulsion droplets to aerosols and observed over an order of magnitude enhancement in reactivity for droplets with air–water interfaces compared to those surrounded by oil. This work also highlighted, by employing a single reaction in two distinct microenvironments, the importance of the confining interface (oil/water vs. air/water) for the overall acceleration of reaction kinetics. This is perhaps not surprising since there are key physicochemical differences between the oil–water and air–water interfaces, particularly in the strength of the interfacial hydrogen bonding network and zeta potential, suggesting that chemical reactivity could vary significantly between these interfacial environments.[30,31] Going beyond microdroplets with air–aqueous interfaces, we examine the reactivity and properties of the oil–water interface of microcompartments to further expand our understanding of how the nature of the confining interface alters microscale reaction kinetics.

Pyruvic acid (PA), a simple α-keto acid, has become a model system for the study of unique interfacial chemistry at the air–water interface.[15,16,32–34] PA is prevalent in both atmospheric aerosol and cells, playing an important role in regulating chemistry through secondary organic aerosol production and metabolic regulation.[35–38] In bulk solutions, PA spontaneously undergoes a self-reaction to form zymonic acid (ZA), a butanolide, and water. The net reaction, neglecting potential intermediates such as parapyruvic acid, is:

particle partitioning whereby the reaction is quenched when evaporation of PA and water are eliminated.[32]

Kim et al.[16] investigated this reaction in aqueous aerosols ($r \sim$ 240 nm) in a series of flow tube reactors. The reaction is observed to be second order and proceeded at the interface with a rate coefficient that is 10^4 larger than in a bulk macroscale solution.[16] Although the studies by Li et al.[15,32] and Kim et al.[16] demonstrate significant reaction acceleration in microdroplets, the reaction mechanism (autocatalytic vs. second order) is uncertain, suggesting many open questions still remain as to how the interface facilitates ZA formation. Comparing the reactivity of PA in microcompartments with air–water and oil–water interfaces provides additional insights into the factors governing reaction dynamics at aqueous interfaces and in microdroplets.

In this work, we investigate the condensation of PA at the oil–water interface using water-in-oil emulsions. Using microfluidics and optical trapping of single micron-sized emulsion droplets, reaction kinetics of ZA formation are measured in situ using Raman spectroscopy. Significant ZA is formed, which when analyzed using a kinetic model quantifies the contribution of interfacial partitioning and surface reactivity to the overall observed kinetics. Interfacial tension measurements (IFT) are used to constrain interfacial partitioning, leaving the interfacial reaction rate coefficient the only free parameter in the model. Lastly, we compare the observed reactivity in emulsions to previous studies at the air–water interface, where we observe enhanced reactivity at the oil–water interface despite reduced interfacial partitioning, providing more general insights into how interfacial composition and partitioning influence condensation reactions in microcompartments.

In macroscale aqueous solutions, the reaction is extremely slow; occurring over months under strongly acidic conditions.[39,40] Li et al.[15,32] investigated the reactivity of PA in sessile droplets (radius, $r = 100–400$ microns) deposited on a hydrophobic slide. They observed significantly enhanced kinetics at the air–water interface that produced 10^6 times faster reaction rates than observed in a bulk macroscale solution. In these droplets, ZA appeared to be formed by an autocatalytic mechanism and the reaction exhibited a strong sensitivity to gas-

II. Methods

Aqueous PA water-in-oil emulsions are generated using a flow-focusing junction microfluidic chip (DropChip, Cellix Ltd.). The initial PA concentration in the emulsions matches that of the bulk solution used for their preparation. The oil phase is fluorinated (HFE7500) and contains 2 wt% of a proprietary fluorosurfactant (RAN Biotechnologies). The fluorinated oil and surfactant produce highly stable emulsions with minimal leakage of material from the aqueous phase.[41] After generation,
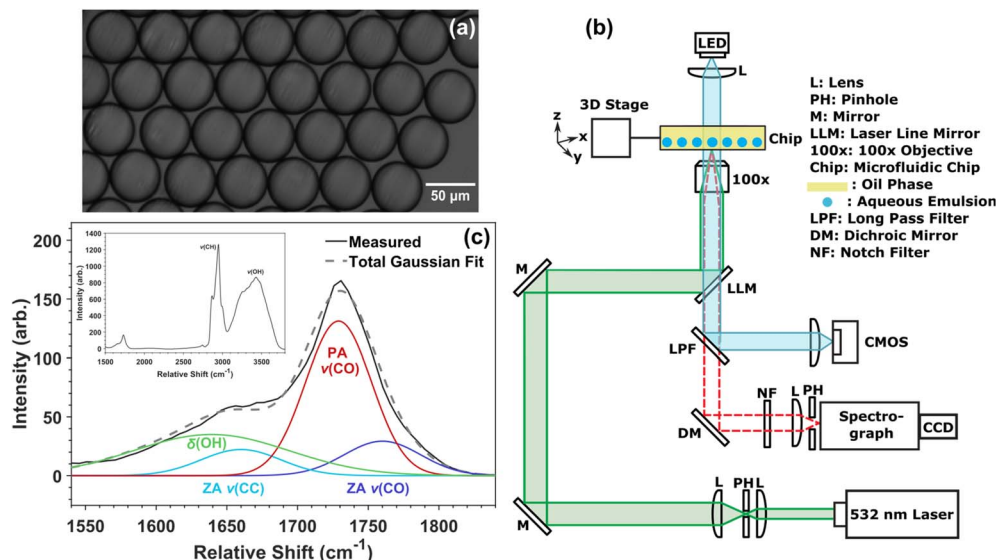
Fig. 1 (a) Image of a set of water-in-oil emulsions used for size variability testing with average radii of 26.1 ± 0.2 μm. (b) Schematic diagram of the optical trap setup used for *in situ* measurements of single optically trapped emulsion droplets. (c) Raman spectrum of a single aqueous PA emulsion droplet with initial PA and ZA concentrations of 1.62 M and 0.25 M, respectively. The deconvolution of the Raman signal between 1540 and 1840 cm^{-1} is shown, where the overall peak comprises C=O stretching for PA, C=C and C=O stretches for ZA, and OH bending from water. The measured Raman spectrum is shown in black, with the fitted spectrum represented by a dashed line. The deconvoluted peaks for PA, ZA, and water are shown in red, light and dark blue, and green, respectively. The inset displays the full Raman spectrum of the emulsion.

emulsions are transported to a storage chip (Vena8 with Glass Coverslips, Cellix Ltd.) with channel dimensions of 40 000 × 800 × 80 μm for *in situ* characterization. Each chip contains ~5000 individual droplets with a standard deviation in radius of ±0.2 μm. Fig. S1† shows this size distribution, while Fig. 1(a) shows an image of emulsions produced by the microchip. Additional details on droplet generation and reproducibility can be found in Section S2 of the ESI.†

Raman spectroscopy of individual emulsion droplets is performed using a modified commercial optical trap (Biral, AOT-100). A *x–y–z* stage was added to the instrument, which allows for 3D manipulation of the microfluidic chips around the stationary trapping laser. A general schematic of the modified system is shown in Fig. 1(b). In a typical measurement, a single emulsion droplet is trapped and isolated from its surrounding droplets. For a single kinetic measurement, Raman spectra are collected from an average of 5 droplets. A sample spectrum of a single emulsion droplet ($r = 28.3 \pm 0.2$ μm, [PA] = 1.62 M, [ZA] = 0.25) is shown in the inset of Fig. 1(c). The intensity in the CH stretching region, centered around 2950 cm^{-1}, arises mainly from the oil and acrylic microchip, and therefore is not used for analysis. The Raman spectra of the oil and chip in the absence of emulsions is shown in Fig. S2.† Outside of the CH stretching region, it is evident there is no Raman signal from the oil phase or the chip itself.

Due to the spontaneous, albeit slow, conversion of PA to ZA in bulk solutions, most commercial samples of PA contain some level of ZA. To accurately identify the Raman stretches of PA without interference from ZA, a small amount of pure PA was obtained *via* distillation. Fig. S3† shows the Raman spectra of PA before and after distillation. The shoulders around

1650 cm^{-1} and 1770 cm^{-1} disappear upon distillation, leaving only a single peak centered at 1729 cm^{-1}, which is assigned to PA and corresponds to ν(C=O).[15]

To assign the Raman bands of ZA, we obtained an authentic standard from the distillation of PA as described by Perkins *et al.*[39] The Raman spectrum of ZA is shown in Fig. S4(d),† and exhibits two prominent peaks corresponding to ν(C=C) at 1660 cm^{-1} and ν(C=O) at 1760 cm^{-1}.[15] There is some overlap of the characteristic bands of PA and ZA, so Gaussian fitting is used to deconvolute individual contributions. PA is represented as a single Gaussian, whereas ZA is represented as two Gaussians, with the amplitude ratio between the C=C and C=O fixed, allowing a single amplitude parameter to fit both bands. An additional Gaussian peak is included to account for water's bending vibration at 1639 cm^{-1}. The Gaussian fitting procedure for PA and ZA standards is detailed in Fig. S4(a) and (d),† respectively. Fig. 1(c) illustrates the contributions of these peaks to the overall Raman signal, which closely replicates the measured spectrum, confirming the accuracy of the fitting procedure.

To quantitatively measure the concentration of PA and ZA, calibration curves of Raman intensity *vs.* concentration are constructed using bulk solutions. Raman intensity for each concentration is quantified using the amplitudes of the fitted Gaussians for PA and ZA relative to the area of the OH stretching band of water (3050–3700 cm^{-1}), as shown in Fig. S4(b) and (e),† respectively. The calibration curves are shown in Fig. S4(c)† for PA and Fig. S4(f)† for ZA. Calibration curves, constructed in units of molality, are converted to molarity through the relationship described in Section S4 of the ESI and shown in Fig. S5.† Additional information on the assignment, Gaussian fitting and bulk calibrations of PA and ZA can also be found in Section S4.†
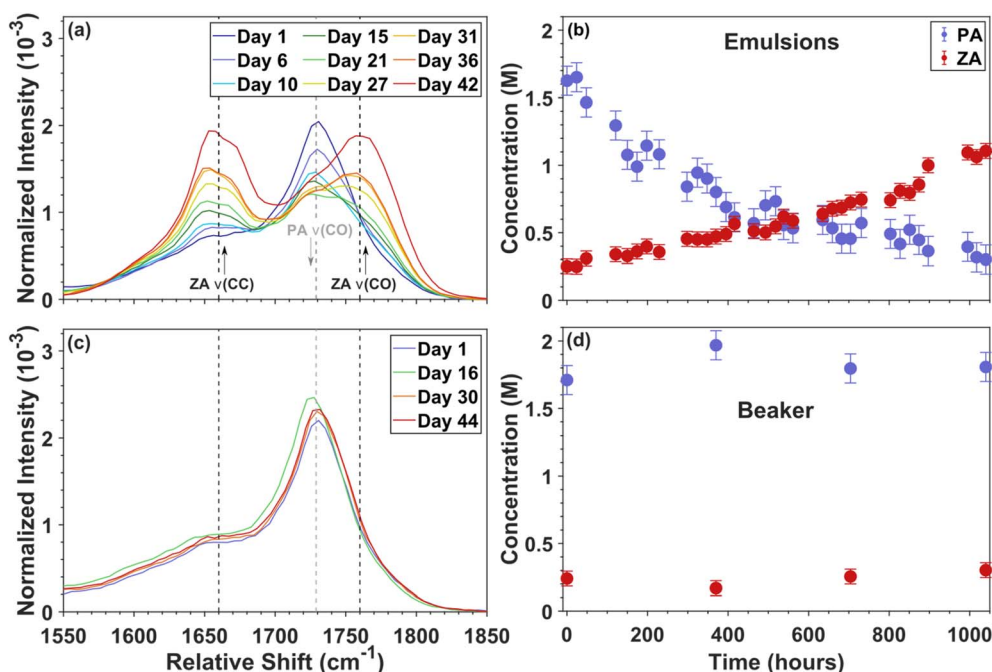
Fig. 2 Raman spectra and kinetics of PA and ZA in emulsions and in bulk. (a) Raman of PA and ZA in emulsion droplets with an initial radius of 28.3 μm over 42 days. The black dashed lines indicate C=C and C=O stretching frequencies of ZA, while the grey dashed line represents the C=O stretch of PA. (b) PA and ZA concentrations in emulsions over time, determined *via* Gaussian fitting of the characteristic Raman peaks in (a). (c) and (d) Bulk experiment using the same PA solution as in (a) and (b), showing Raman spectra over time (c) and PA and ZA concentrations (d). Raman spectra in (a) and (c) are normalized to the intensity of the Raman band of water. The full, raw Raman spectra of emulsions and bulk are shown in Fig. S6(a) and (b),† respectively. Error bars in (c) and (d) represent the uncertainty associated with day-to-day spectral drift of the spectrometer, which was determined by the variability in PA and ZA bulk concentrations over time as shown in (d). The average uncertainty of concentration between the 5 emulsion droplets sampled for each datapoint in (b) was less than ± 0.05 M.

III. Results

Fig. 2(a) shows Raman spectra *vs.* time for aqueous PA emulsion droplets ($r = 28.3$ μm) with an initial PA concentration of 1.62 M. Given the large number of emulsions on the microchip, a different section of the chip is measured each day, ensuring a new set of droplets were analyzed daily to minimize the potential influence of laser irradiation on the observed kinetics. As seen in Fig. 2(a) there is a clear decrease in the C=O stretching band centered at 1729 cm^{-1} indicating that [PA] decreases with time. Correspondingly, there is a rise in the ZA peaks representing the C=C and C=O functional groups centered at 1660 and 1760 cm^{-1}, respectively. The concentration of PA and ZA in the emulsions over approximately 1050 hours (44 days) is shown in Fig. 1(b). Over this time period a significant quantity of ZA (~1 M) is formed.

For direct comparison to the emulsion experiment described above, we measured the concentration of PA and ZA in a macroscale sample over time. This solution is the same one used to generate the emulsions in Fig. 2(a) and (b). The full Raman spectra of the emulsions and macroscale sample are shown in Fig. S6(a) and (b),† respectively. To measure the macroscale kinetics, approximately 5 mL of the aqueous PA solution was stored in a Falcon tube. At regular intervals throughout the 1050 hour duration of the emulsion experiment, 5 μL of the bulk solution was pipetted into a storage chip where

Raman spectra are recorded. The results of the bulk experiment are shown in Fig. 2(c) and (d). At $t = 0$, there is excellent agreement between macroscale and droplet concentrations of PA and ZA. This suggests the oil phase and microfluidic chip itself have a negligible effect on the Raman spectra of PA and ZA and further validates that the bulk calibration curves accurately determine the concentrations in emulsions. After $t = 0$, the bulk concentrations of PA and ZA remain relatively constant for 1050 hours, showing no evidence for a reaction. This is in stark contrast to the emulsion experiment where after 1050 hours ~1 M of ZA is formed.

IV. Kinetic analysis

The results in Fig. 2 clearly demonstrate a substantial increase in the reaction kinetics in emulsions relative to a bulk macroscale solution. To understand the origin of the accelerated formation rate of ZA, a kinetic model is developed where explicit contributions of droplet bulk and interface on the reaction kinetics can be determined.[12,13,42–44] The model is adapted from Kim *et al.*[16] and therefore will only be briefly discussed here. The kinetic model is implemented in the stochastic simulator, Kinetiscope (**https://www.hinsberg.net/kinetiscope/**).[45] For this work, a two compartment model is used to represent the surface and bulk regions of the emulsion droplet.[12] The interface compartment has
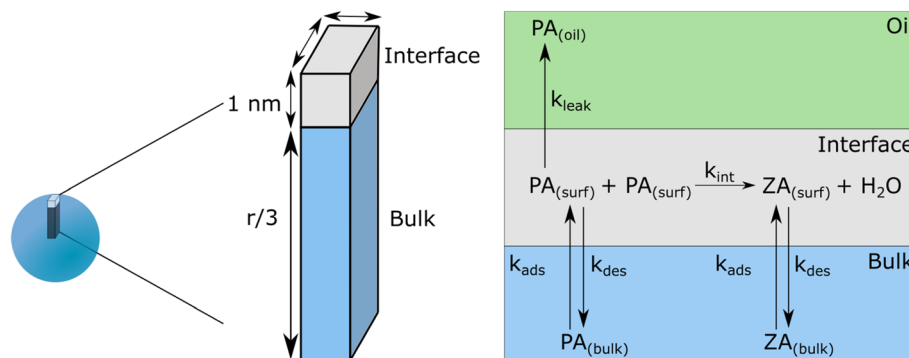
Fig. 3 Schematic of the kinetic model used to simulate the emulsion experiments. The spherical emulsion droplet is represented as a box model, consisting of a bulk compartment ($1 \times 1 \times r/3$ nm^3) and a surface compartment ($1 \times 1 \times 1$ nm^3). The model accounts for PA and ZA partitioning between the interface and bulk, an interfacial reaction, and leakage into the oil phase. All parameters used in the model are presented in Table S1.†

a thickness of 1 nm, which is consistent with the density profile at the oil–water interface in Molecular Dynamics simulations.[46] The simulation geometry consists of a rectangular prism as shown in Fig. 3. To preserve the correct scaling of surface-to-bulk of a sphere in a rectangular prism, the bulk compartment length is set to $r/3$, where r is the average radius of the emulsion droplet. A schematic of the model, and relevant parameters are shown in Fig. 3. The model is intended to quantitatively account for the surface-bulk partitioning of PA and ZA, as well as the leakage of PA into the oil phase. As will be described below, the only remaining free parameter in the model is the interfacial reaction rate (k_{int}), which is obtained through a best fit to the experimental data.

Dynamic and static interfacial tension (IFT) measurements constrain the rate of surface adsorption (k_{ads}), desorption (k_{des}) of PA, the equilibrium surface partitioning constant (K_{eq}) and the maximum surface concentration of PA (Γ_∞). In the absence of data for ZA, we apply these same partitioning parameters that are obtained for PA. A description of the IFT experiments and the results are summarized in Section S5 and Fig S7.† The IFT was measured using the microfluidic platform and pendant drop method. From the equilibrium IFT data, the PA behavior at different concentrations on the oil–water interface is characterized by using Langmuir isotherm models, as described in Section S5,† to determine the maximum surface concentration and the equilibrium surface partitioning of PA. In addition, the dynamic IFT measured using the microfluidic device is used to obtain the kinetic parameters associated with interfacial adsorption.

To accurately constrain the potential leakage rate of PA into the oil phase, given the long timescale of the measurements, control experiments were performed using a non-reactive surrogate for PA. Acetic acid (AA) is used for these measurements since it has similar functionality and an oil–water partitioning coefficient to PA.[47] Experiments and kinetic modelling of AA leakage at 3 different concentrations, using only a single bulk oil–water partitioning coefficient yielded excellent agreement for both the size and concentration profile over time. The results of the leakage experiment and model are

summarized in Fig. S8 and discussed in more detail in Section S6.† The parameters used in the kinetic model are shown in Table S1.†
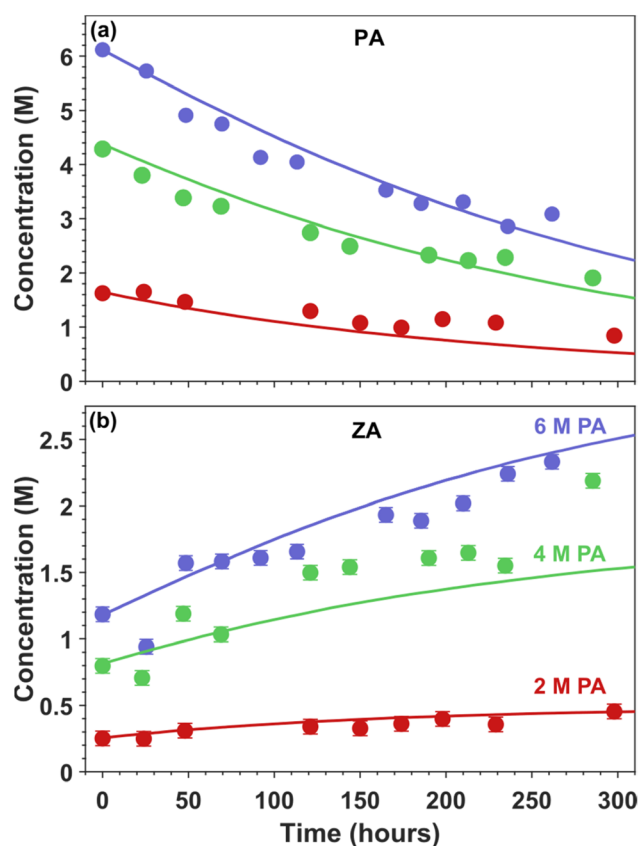

Fig. 4 Kinetics of PA (a) and ZA (b) for emulsions with initial PA concentrations of 6.12 M (purple), 4.29 M (green), 1.63 M (red). The experimental data is represented as the points and the solid lines correspond to the kinetic model. In (a) the error bars determined by either spectral drift, as shown in Fig. 2(b) for bulk measurements (±0.11 M) or standard deviation across the 5 emulsion droplets measured for each datapoint (±0.05 M) is both smaller than the datapoints, thus no error bars are present. In (b) the error bars represent the day-to-day uncertainty from spectral drift of the spectrometer.

The ZA formation rate in emulsions was investigated at three different initial PA concentrations. To obtain the interfacial reaction rate constant, the kinetic model is fit to the experimental data. Fig. 4(a) summarizes the PA kinetics over time, while Fig. 4(b) shows the ZA formation kinetics. For the experimental measurements summarized in Fig. 4, the difference in radii of the three emulsion sets were kept to within ± 1 μm to minimize size effects on the reaction. The initial radii for the emulsion droplets in Fig. 3 are 27.5 μm for [PA] = 6.12 M, 28.5 μm for [PA] = 4.29 M, and 28.3 μm for [PA] = 1.62 M. At all three initial PA concentrations, significant ZA formation was observed. For the initial PA concentrations of 6.12 and 4.29 M, over 1 M of ZA was formed within 300 hours. For the lowest initial PA concentration (1.62 M), ∼0.2 M of ZA was produced, which is markedly less than the more concentrated emulsions. Notably, no significant ZA formation is seen in the macroscale samples over the same period for any of the initial PA concentrations, as shown in Fig. 2(d). The kinetic model, fitting the surface reaction rate coefficient to the experimental measurements in Fig. 4, is shown in the solid lines. The model replicates all of the experimental results using a single surface reaction rate coefficient of $(1.8 \pm 0.2) \times 10^{-2}$ M^{-1} s^{-1}. Although there is no reported rate coefficient for a bulk solution under our experimental conditions, the acid catalyzed reaction has been investigated previously, with an estimated rate coefficient of 4×10^{-8} M^{-1} s^{-1}.[16,40] Thus relative to the macroscale, the rate coefficient for ZA formation at the oil–water interface is larger by 5 orders of magnitude.

During the 300 hour reaction time, the emulsion droplets gradually shrink from both leakage of PA into the oil-phase and density changes that accompany the reaction. The change in emulsion droplet size with time are shown in Fig. S9,† along with the model predictions. The model captures the size evolution for [PA] = 6.12 M and 1.63 M, but underestimates the size decrease at [PA] = 4.29 M. Since the overall reaction rate is expected to scale as inverse radius $(1/r)$,[12] the enhanced size reduction for the 4.29 M data relative to the model likely contributes to the difference between the model and observations of ZA formation in Fig. 4(b).

V. Discussion

We first examine enhanced ZA formation in emulsions compared to bulk solutions, exploring potential pathways for acceleration at the interface and compare the observed acceleration factor to a previous study on condensation reactions in emulsions. We then examine the differences in partitioning behavior and surface reactivity of PA between the oil–water and air–water interfaces. Finally, we integrate these findings into kinetic modelling to directly compare the overall reactivity in emulsion droplets to droplets in air, thereby analyzing the interplay between partitioning and surface reactivity in governing the observed reaction kinetics.

The surface reaction rate constant for ZA formation at the oil–water interface in this work $(1.8 \times 10^{-2}$ M^{-1} s$^{-1})$ is 5 orders of magnitude larger than the estimated bulk rate of 4×10^{-8} M^{-1} s^{-1}.[16,4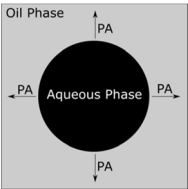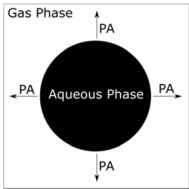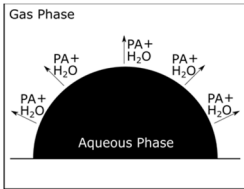0] This substantial enhancement highlights the unique reaction environment of the interface, which can drive accelerated chemistry. For this condensation reaction, the most likely cause for the enhancement is partial solvation, which is consistent with previous studies showing accelerated condensation reactions in microcompartments, such as imine synthesis and peptide bond formation.[1,19,48,49] In this partially solvated environment, transition state stabilization may lower the activation energy required for the reaction to proceed.[20] To the best of our knowledge, there has only been one other study on condensation reaction enhancement in emulsions.[1] Fallah-Araghi et al.,[1] investigated imine synthesis in emulsions, where kinetic modeling determined a surface reaction rate of 10^{-3} M^{-1} s^{-1},[12] which is similar in magnitude to the interfacial rate (i.e., 10^{-2} M^{-1} s^{-1}) reported here. The similarity between these interfacial rates further supports the idea that partial solvation at the interface favors condensation reactions. However, a striking difference between our work and that of Fallah-Araghi et al.[1] lies in the acceleration factor relative to the bulk rate. While their work reported a relatively modest 50× enhancement, our result suggests a much larger acceleration factor (i.e., 5×10^5). This discrepancy is likely due to differences in reaction mechanism or the molecular structure of the reactants, as Fallah-Araghi et al.[1] utilized large reactant molecules to form a fluorescent product, which may have been sterically hindered at the interface compared to the relatively small size of PA.

In this work, it is worth noting that the oil–water interface also contains surfactant molecules. It is possible that the fluorinated surfactant could be important in controlling the reactivity and partitioning behavior at the interface. The presence of the surfactant could stabilize a reaction intermediate, or product, potentially through steric effects or intermolecular interactions, leading to enhanced reactivity. While not a direct comparison, enhanced reactivity has been observed in emulsions stabilized by solid catalytic particles, most commonly palladium-based, adsorbed at the interface, known as Pickering emulsions.[50–54] Alternatively, the presence of surfactant may compete with PA for surface adsorption sites, potentially limiting interfacial concentrations relative to a surfactant-free interface. These ideas are supported by Prophet et al.,[55] who demonstrated suppression of iodide oxidation at the air–water interface through addition of a surfactant. Future work would be necessary to determine the exact role of the surfactant in influencing interfacial chemistry in emulsions.

The rate of ZA formation for the two studies at the air–water interface, as well as the surface rate constant in this study, are summarized in Table 1. Li et al.[32] propose two simultaneous reactions at the air–water interface: direct ZA formation from PA and a step wherein ZA formation from PA is catalyzed by ZA itself. In Table 1, the reaction rate obtained from sessile droplets from Li et al.[32] is the uncatalyzed rate and is 10^{-1} M^{-1} s^{-1}. Kim et al.[16] report a rate for aqueous nanodroplets on the order of 10^{-3} M^{-1} s^{-1}. The value determined here for microemulsions $(1.8 \times 10^{-3}$ M^{-1} s$^{-1})$ lies between these values, suggesting potential mechanistic similarities and differences between the two interfaces.

Table 1 Comparison of interfacial partitioning and reactivity for PA at the oil–water and air–water interface. A simple schematic of experimental conditions is also shown, highlighting PA loss into the oil and gas for this this work and Kim et al.,[16] respectively and PA and associated water loss into the gas phase for Li et al.[32] The surface rate from Li et al. was converted from units of molality using the density of aqueous PA at 4.3 molal, which was the concentration used in most of their experiments. In Li et al. bulk-to-surface partitioning was not explicitly considered, therefore it is listed as bulk in the table

	Oil–water	Air–water (Kim et al.[16])	Air–water (Li et al.[32])
Γ_∞ (mol cm^{-2})	$(1.7 \pm 1.3) \times 10^{-10}$	4.3×10^{-10}	Bulk
K_{eq} (M^{-1})	0.17 ± 0.16	28.5	Bulk
k_{int} (M^{-1} s^{-1})	$(1.8 \pm 0.2) \times 10^{-2}$	0.9×10^{-3}	2.36×10^{-1}
Radius (μm)	28.1	0.24	$100–500$
Experimental conditions			

While these rate constants provide a useful point of comparison, a closer look at the underlying experimental conditions reveals key mechanistic differences. For reference, a simple schematic of the experimental conditions of each experiment is summarized in Table 1. Li et al.,[15,32] observed sigmoidal reaction kinetics, consistent with the autocatalytic mechanism suggested above. They argued that the autocatalytic step is a result of PA evaporation and corresponding water loss, resulting in amplification of the ZA concentration, which is self-catalyzing. Interestingly, when Li et al.[15,32] inhibit PA evaporation, the reaction ceased completely over the course of their 500 minute experiment. In both this work, and the study by Kim et al.,[16] loss of PA occurs either through leaking directly into the oil, or through evaporation into the gas-phase, respectively. However, the key difference in these studies compared to Li et al.[15,32] is the absence of water loss and the associated sigmoidal kinetics (i.e., autocatalysis). To investigate this further, we compared predictions from our kinetic model and the model reported by Kim et al.,[16] to the measured kinetics of ZA formation from Li et al.[15,32] To do this we turned off both PA and water evaporation. The results are shown in Fig. S10.† The experimental data and model predictions are consistent and clearly show that after 500 minutes, no ZA is detected. Both models predict very small quantities of ZA (<7 mM) formed during this time period, which would be undetectable by Raman spectroscopy used by Li et al.[15,32] If these experiments (without water evaporation) were run for longer, such as 300 hours, as is done here, we expect Li et al.[15,32] would observe ZA formation with similar reaction kinetics to that reported here and in Kim et al.[16] Therefore, it is difficult to compare our results at the oil–water interface directly to the work of Li et al.[15,32] given the catalytic role of water loss in their experiments that is absent in our work.

In contrast, our experimental conditions are more directly comparable to those of Kim et al.[16] At the oil–water interface, the surface rate constant is 20 times higher than their reported value for the air–water interface. The reason for the difference is currently unclear but may reflect differences in the aqueous phase composition. For example, Kim et al.,[16] used salt ([NaCl] = 4.6 M) to control the droplet's water activity (i.e., to prevent water evaporation). Thus, the difference in these interfacial rate coefficients may simply reflect differences in ionic strength. Alternatively, enhanced reactivity at the oil–water interface could arise from a fundamentally different interfacial reaction environment. Stabilization of reaction intermediates may result from the presence of a surfactant, the surrounding oil phase, interfacial zeta potentials, or distinct properties of interfacial water itself, such as altered hydrogen bonding networks. Further fundamental studies that directly probe these interfacial properties, such as experimental techniques including vibrational sum-frequency spectroscopy, for example, and computational approaches including molecular dynamics simulations, will be essential to identify the underlying mechanisms.[30,56–58]

Although the interfacial rate coefficient plays a crucial role in enhancing reaction rates within microcompartments, interfacial partitioning of reactants/products also govern the observed reaction rates.[11,12,59] In Table 1, we compare the partitioning behavior of PA at the oil–water and air–water interfaces directly. The study by Li et al.[32] neglects bulk-interface partitioning, therefore we only compare the partitioning of PA at the oil–water interface to Kim et al.[16] at the air–water interface. Surprisingly, the IFT measurements indicate significantly lower surface activity of PA at the oil–water interface compared to the air–water interface. The equilibrium interfacial partitioning coefficient of PA at the oil–water interface is over 100 times smaller than the air–water interface. Additionally, the maximum surface coverage of PA at the oil–water interface is approximately 2.5 times lower than at the air–water interface. These differences are likely due in part to the competitive adsorption of PA with the fluorosurfactant used to stabilize the emulsions.
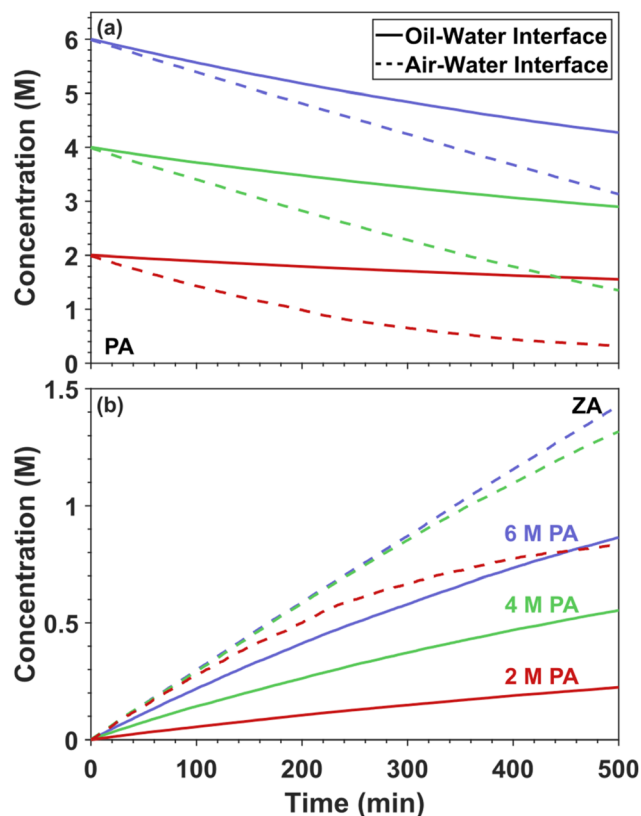
Fig. 5 Kinetic model comparison of PA (a) and ZA (b) reaction kinetics at the oil−water (solid lines) and air−water (dashed lines) interfaces for initial PA concentrations of 6 M (purple) 4 M (green) and 2 M (red). Simulations were performed with an initial droplet radius of 1 μm. For direct comparison, PA leakage in emulsions and evaporation in aerosols were excluded from the model.

In the remaining discussion we examine how partitioning and surface reactivity contribute to the observed reaction rate for droplets in air and emulsion droplets by comparing the kinetic models directly. The observed kinetics, turning off evaporation of PA at the air−water and leakage into the oil-phase for the oil−water, are shown in Fig. 5(a) for PA and Fig. 5(b) for ZA. The simulations are performed for a droplet with an initial

radius of 1 μm at three different initial concentrations. In Fig. 5(b) it is evident that for droplets in air significantly more ZA is produced. This difference relative to emulsions is most pronounced at the lowest PA concentration, with 3.72 times more ZA produced in air at [PA] = 2 M, followed by 2.38 times more at [PA] = 4 M and 1.65 times more at [PA] = 6 M. The enhanced reactivity of droplets in air persists despite the air−water interface being 20× less reactive than the oil-water interface. This difference is explained in Fig. 6(a), which shows the equilibrium surface concentration of PA at the oil−water and air−water interface. The equilibrium surface concentrations were calculated using the Langmuir isotherm as described in Section S5 of the ESI† using the equilibrium IFT at different PA concentrations. For emulsions, the surface concentration is significantly less than the bulk. A common argument for enhanced interfacial chemistry is the excess concentration of surface-active reactants at the interface relative to bulk solutions.[10] However, in this case, overall reaction enhancement in emulsions occurs despite the lower concentration of PA at the interface compared to bulk. For droplets in air, the surface concentration is always higher than the bulk until the surface becomes saturated at 4.3 M, as demonstrated in Fig. 6(a). Although the reactivity at the oil−water interface is much larger, the overall quantity of PA at the interface available to react is significantly less; slowing down the overall reaction rate. This is further highlighted in Fig. 6(b) and (c), which show the time-dependent surface concentrations of PA during the reaction at the oil−water and air−water interfaces, respectively. During the reaction in emulsions, the surface never reaches its maximum surface coverage, even at 6 M bulk concentration, and slowly decreases over time. This is also the case for the lower bulk concentrations, which each begin with lower initial surface concentrations.

In contrast, the air−water interface exhibits a much different profile during the reaction. At the beginning of the reaction, at all initial bulk concentrations, the air−water interface is saturated (i.e., at its maximum surface concentration). It should be noted that for the air−water case, the temporal decrease in surface PA concentration is a result of competitive adsorption with ZA. The surface concentrations of ZA at the oil-water and
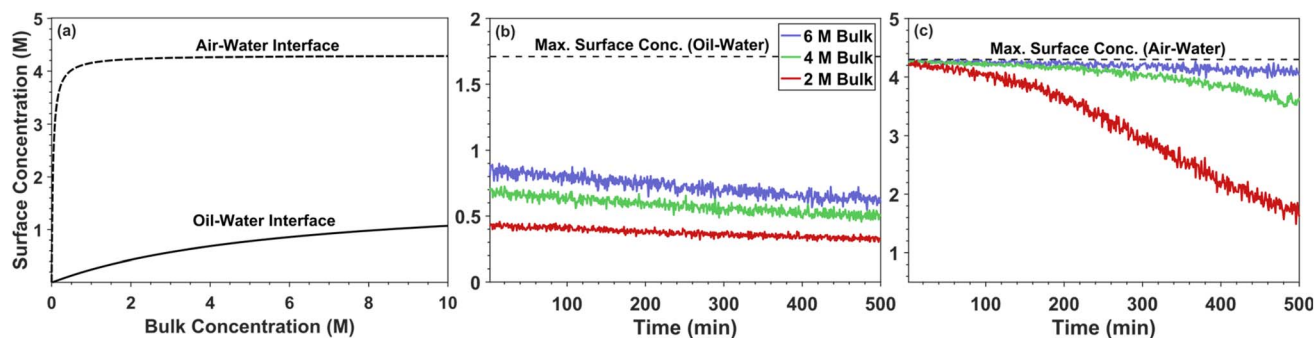

Fig. 6 Comparison of PA surface partitioning at the oil-water and air−water interfaces. (a) Equilibrium surface concentrations of PA with respect to bulk concentration at the oil−water interface (solid line) and air−water interface (dashed line). (b) Surface concentration of PA at the oil−water interface over time for the reactions highlighted in Fig. 5, with initial PA concentrations of 6 M (purple), 4 M (green) and 2 M (red). The dashed line represents the maximum surface concentration of PA at the oil−water interface. (c) Surface concentration of PA at the air−water interface over time for the same reactions. The dashed line indicates the maximum surface concentration of PA at the air−water interface.

air–water interface are shown in Fig. S11(a) and (b),† respectively. As ZA is formed, it will occupy a portion of surface sites and displace PA. This is most notable for the 2 M PA droplet, where at the end over 1 M of ZA occupies the interface, resulting in a final PA concentration at the interface less than 2 M (Fig. 6(c)). At all times throughout the reaction, the surface concentration at the air–water interface was at least $5\times$ more concentrated than the oil–water interface at a given bulk concentration, which allows the overall reaction to proceed more efficiently than the emulsions, overcoming the reduced interfacial reactivity.

This analysis clearly highlights the interplay between interfacial reactivity and partitioning in governing overall droplet reactivity, and the importance in understanding differences between interfacial regimes. Recently, Krushinski et al.[29] compared enzyme reactivity in emulsions and aerosols, reporting over an order of magnitude enhancement for droplets in air. They attributed this enhancement to a more reactive air–water interface relative to the oil–water interface. As demonstrated here, however, without disentangling the contributions of partitioning and interfacial reactivity (i.e. the rate constant) it is difficult to discern the origin of enhanced chemistry at different interfaces. It is possible that the reduced overall reaction in emulsions observed in their work could also be a result of hindered interfacial partitioning, rather than a less reactive interface.

VI. Conclusions

In this work, we demonstrated enhanced PA reactivity at the oil–water interface relative to macroscopic bulk solutions and the air–water interface, leading to efficient ZA formation. This was achieved using microfluidics, optical trapping and Raman spectroscopy for in situ probing of in-droplet chemistry. The rate constant for ZA formation at the oil-water interface is determined to be approximately five orders of magnitude larger than in bulk. Through the development of a kinetic model, explicitly incorporating bulk-to-surface partitioning and surface reactivity, we compared our findings to previous studies at the air–water interface. At the oil–water interface, PA reaction kinetics were accelerated $20\times$ compared to the air–water interface. This result highlights fundamentally different reaction environments at the two interfacial regimes and should promote many further investigations. Despite the reduced reactivity at the air–water interface, overall ZA formation was significantly more efficient in droplets in air compared to emulsion droplets due to the markedly lower interfacial partitioning in emulsions, highlighting the critical interplay between surface reactivity and partitioning in governing reaction kinetics within microcompartments.

Data availability

Data are available from the corresponding author upon request.

Author contributions

Project conceptualization: B. J. W., K. R. W. and A. A. Emulsion and bulk Raman experiments and data analysis: B. J. W. IFT experimentation and data analysis: M. M., R. B. and C. S. D. Kinetic modelling: B. J. W., P. K., K. R. W. and M. A. Original draft preparation: B. J. W. Draft editing and review: all authors.

Conflicts of interest

There are no conflicts of interest to declare.

Acknowledgements

References

1 A. Fallah-Araghi, K. Meguellati, J.-C. Baret, A. E. Harrak, T. Mangeat, M. Karplus, S. Ladame, C. M. Marques and A. D. Griffiths, Enhanced Chemical Synthesis at Soft Interfaces: A Universal Reaction-Adsorption Mechanism in Microcompartments, Phys. Rev. Lett., 2014, 112, 028301.

2 A. Logozzo, B. Vennes, R. Kaur Kohli, J. F. Davies, D. J. Castillo-Pazos, C. J. Li, C. D. Neish and T. C. Preston, Photochemically Driven Peptide Formation in Supersaturated Aerosol Droplets, Angew. Chem., Int. Ed., 2024, 63, e202409788.

3 Z. Wei, Y. Li, R. G. Cooks and X. Yan, Accelerated Reaction Kinetics in Microdroplets: Overview and Recent Developments, Annu. Rev. Phys. Chem., 2020, 71, 31–51.

4 E. K. Brown, G. Rovelli and K. R. Wilson, pH jump kinetics in colliding microdroplets: accelerated synthesis of azamonardine from dopamine and resorcinol, Chem. Sci., 2023, 14, 6430–6442.

5 J. K. Lee, S. Banerjee, H. G. Nam and R. N. Zare, Acceleration of reaction in charged microdroplets, Q. Rev. Biophys., 2015, 48, 437–444.

6 X. Yan, R. M. Bain and R. G. Cooks, Organic reactions in microdroplets: reaction acceleration revealed by mass spectrometry, Angew. Chem., Int. Ed., 2016, 55, 12960–12972.

7 R. M. Bain, C. J. Pulliam, F. Thery and R. G. Cooks, Accelerated chemical reactions and organic synthesis in Leidenfrost droplets, Angew. Chem., Int. Ed., 2016, 55, 10478–10482.

8 M. T. C. Martins-Costa and M. F. Ruiz-López, Electrostatics and Chemical Reactivity at the Air–Water Interface, *J. Am. Chem. Soc.*, 2023, **145**, 1400–1406.

9 G. Rovelli, M. I. Jacobs, M. D. Willis, R. J. Rapf, A. M. Prophet and K. R. Wilson, A critical analysis of electrospray techniques for the determination of accelerated rates and mechanisms of chemical reactions in droplets, *Chem. Sci.*, 2020, **11**, 13026–13043.

10 M. F. Ruiz-Lopez, J. S. Francisco, M. T. C. Martins-Costa and J. M. Anglada, Molecular reactions at aqueous interfaces, *Nat. Rev. Chem.*, 2020, **4**, 459–475.

11 M. F. Ruiz-López and M. T. Martins-Costa, Disentangling reaction rate acceleration in microdroplets, *Phys. Chem. Chem. Phys.*, 2022, **24**, 29700–29704.

12 K. R. Wilson, A. M. Prophet, G. Rovelli, M. D. Willis, R. J. Rapf and M. I. Jacobs, A kinetic description of how interfaces accelerate reactions in micro-compartments, *Chem. Sci.*, 2020, **11**, 8533–8545.

13 K. R. Wilson and A. M. Prophet, Chemical Kinetics in Microdroplets, *Annu. Rev. Phys. Chem.*, 2024, **75**, 185–208.

14 T. Müller, A. Badu-Tawiah and R. G. Cooks, Accelerated carbon-carbon bond-forming reactions in preparative electrospray, *Angew. Chem., Int. Ed.*, 2012, **51**, 11832–11835.

15 M. Li, C. Boothby, R. E. Continetti and V. H. Grassian, Size-Dependent Sigmoidal Reaction Kinetics for Pyruvic Acid Condensation at the Air–Water Interface in Aqueous Microdroplets, *J. Am. Chem. Soc.*, 2023, **145**, 22317–22321.

16 P. Kim, R. S. Reynolds, A. M. Deal, V. Vaida, M. Ahmed and K. R. Wilson, Accelerated Zymonic Acid Formation from Pyruvic Acid at the Interface of Aqueous Nanodroplets, *J. Phys. Chem. Lett.*, 2024, **15**, 11131–11138.

17 Y. Li, X. Yan and R. G. Cooks, The Role of the Interface in Thin Film and Droplet Accelerated Reactions Studied by Competitive Substituent Effects, *Angew. Chem., Int. Ed.*, 2016, **55**, 3433–3437.

18 D. T. Holden, N. M. Morato and R. G. Cooks, Aqueous microdroplets enable abiotic synthesis and chain extension of unique peptide isomers from free amino acids, *Proc. Natl. Acad. Sci. U. S. A.*, 2022, **119**, e2212642119.

19 E. C. Griffith and V. Vaida, In situ observation of peptide bond formation at the water–air interface, *Proc. Natl. Acad. Sci. U. S. A.*, 2012, **109**, 15697–15701.

20 L. Qiu, Z. Wei, H. Nie and R. G. Cooks, Reaction acceleration promoted by partial solvation at the gas/solution interface, *ChemPlusChem*, 2021, **86**, 1362–1365.

21 F. Goodarzi and S. Zendehboudi, A Comprehensive Review on Emulsions and Emulsion Stability in Chemical and Energy Industries, *Can. J. Chem. Eng.*, 2019, **97**, 281–309.

22 J. Bibette, F. L. Calderon and P. Poulin, Emulsions: basic principles, *Rep. Prog. Phys.*, 1999, **62**, 969.

23 A. Engel, H. W. Bange, M. Cunliffe, S. M. Burrows, G. Friedrichs, L. Galgani, H. Herrmann, N. Hertkorn, M. Johnson, P. S. Liss, *et al.*, The Ocean's Vital Skin: Toward an Integrated Understanding of the Sea Surface Microlayer, *Front. Mar. Sci.*, 2017, **4**, 165.

24 M. Luo, A. C. Dommer, J. M. Schiffer, D. J. Rez, A. R. Mitchell, R. E. Amaro and V. H. Grassian, Surfactant Charge Modulates Structure and Stability of Lipase-Embedded Monolayers at Marine-Relevant Aerosol Surfaces, *Langmuir*, 2019, **35**, 9050–9060.

25 A. R. Metcalf, N. Shweta and C. S. and Dutcher, A review of microfluidic concepts and applications for atmospheric aerosol science, *Aerosol Sci. Technol.*, 2018, **52**, 310–329.

26 T. Tadros, Application of rheology for assessment and prediction of the long-term physical stability of emulsions, *Adv. Colloid Interface Sci.*, 2004, **108–109**, 227–258.

27 G. M. Whitesides, The origins and the future of microfluidics, *Nature*, 2006, **442**, 368–373.

28 M. I. Jacobs, E. R. Jira and C. M. Schroeder, Understanding How Coacervates Drive Reversible Small Molecule Reactions to Promote Molecular Complexity, *Langmuir*, 2021, **37**, 14323–14335.

29 L. E. Krushinski, P. J. Herchenbach and J. E. Dick, The gas|liquid interface eclipses the liquid|liquid interface for glucose oxidase rate acceleration in microdroplets, *Proc. Natl. Acad. Sci. U. S. A.*, 2024, 121.

30 S. Pullanchery, S. Kulik, B. Rehl, A. Hassanali and S. Roke, Charge transfer across C–H···O hydrogen bonds stabilizes oil droplets in water, *Science*, 2021, **374**, 1366–1370.

31 L. Shi, R. A. LaCour, N. Qian, J. P. Heindel, X. Lang, R. Zhao, T. Head-Gordon and W. Min, Water structure and electric fields at the interface of oil droplets, *Nature*, 2025, **640**, 87–93.

32 M. Li, S. Yang, M. Rathi, S. Kumar, C. S. Dutcher and V. H. Grassian, Enhanced condensation kinetics in aqueous microdroplets driven by coupled surface reactions and gas-phase partitioning, *Chem. Sci.*, 2024, **15**, 13429–13441.

33 K. J. Kappes, A. M. Deal, M. F. Jespersen, S. L. Blair, J.-F. Doussin, M. Cazaunau, E. Pangui, B. N. Hopper, M. S. Johnson and V. Vaida, Chemistry and Photochemistry of Pyruvic Acid at the Air–Water Interface, *J. Phys. Chem. A*, 2021, **125**, 1036–1049.

34 A. E. Reed Harris, A. Pajunoja, M. Cazaunau, A. Gratien, E. Pangui, A. Monod, E. C. Griffith, A. Virtanen, J.-F. Doussin and V. Vaida, Multiphase Photochemistry of Pyruvic Acid under Atmospheric Conditions, *J. Phys. Chem. A*, 2017, **121**, 3327–3339.

35 A. G. Carlton, B. J. Turpin, H. J. Lim, K. E. Altieri and S. Seitzinger, Link between isoprene and secondary organic aerosol (SOA): pyruvic acid oxidation yields low volatility organic acids in clouds, *Geophys. Res. Lett.*, 2006, **33**, L06822.

36 E. C. Griffith, B. K. Carpenter, R. K. Shoemaker and V. Vaida, Photochemistry of aqueous pyruvic acid, *Proc. Natl. Acad. Sci. U. S. A.*, 2013, **110**, 11714–11719.

37 L. R. Gray, S. C. Tompkins and E. B. Taylor, Regulation of pyruvate metabolism and human disease, *Cell. Mol. Life Sci.*, 2014, **71**, 2577–2604.

38 J. T. Pronk, H. Yde Steensma and J. P. Van Dijken, Pyruvate metabolism in Saccharomyces cerevisiae, *Yeast*, 1996, **12**, 1607–1633.

39 R. J. Perkins, R. K. Shoemaker, B. K. Carpenter and V. Vaida, Chemical Equilibria and Kinetics in Aqueous Solutions of Zymonic Acid, *J. Phys. Chem. A*, 2016, **120**, 10096–10107.

40 S. Düwel, C. Hundshammer, M. Gersch, B. Feuerecker, K. Steiger, A. Buck, A. Walch, A. Haase, S. J. Glaser, M. Schwaiger and F. Schilling, Imaging of pH in vivo using hyperpolarized 13C-labelled zymonic acid, *Nat. Commun.*, 2017, **8**, 15126.

41 J.-C. Baret, Surfactants in droplet-based microfluidics, *Lab Chip*, 2012, **12**, 422–433.

42 A. A. Wiegel, K. R. Wilson, W. D. Hinsberg and F. A. Houle, Stochastic methods for aerosol chemistry: a compact molecular description of functionalization and fragmentation in the heterogeneous oxidation of squalane aerosol by OH radicals, *Phys. Chem. Chem. Phys.*, 2015, **17**, 4398–4411.

43 A. M. Prophet, K. Polley, E. K. Brown, D. T. Limmer and K. R. Wilson, Distinguishing Surface and Bulk Reactivity: Concentration-Dependent Kinetics of Iodide Oxidation by Ozone in Microdroplets, *J. Phys. Chem. A*, 2024, **128**, 8970–8982.

44 M. D. Willis and K. R. Wilson, Coupled Interfacial and Bulk Kinetics Govern the Timescales of Multiphase Ozonolysis Reactions, *J. Phys. Chem. A*, 2022, **126**, 4991–5010.

45 W. D. Hinsberg and F. A. Houle, *Kinetiscope-A Stochastic Kinetics Simulator*, **https://hinsberg.net/kinetiscope/**, accessed 2025-01-21.

46 C. Herdes, Å. Ervik, A. Mejía and E. A. Müller, Prediction of the water/oil interfacial tension from molecular simulations using the coarse-grained SAFT-γ Mie force field, *Fluid Phase Equilib.*, 2018, **476**, 9–15.

47 R. Collander, M. Lindholm and C. M. Haug, The partition of organic compounds between higher alcohols and water, *Acta Chem. Scand.*, 1951, **5**, 774–780.

48 A. M. Deal, R. J. Rapf and V. Vaida, Water–Air Interfaces as Environments to Address the Water Paradox in Prebiotic Chemistry: A Physical Chemistry Perspective, *J. Phys. Chem. A*, 2021, **125**, 4929–4942.

49 D. Xia, F. Zeng, W. Chen, H. Zhao, H.-b. Xie, J. Chen and J. S. Francisco, Accelerated peptide bond formation at air–water interfaces, *Proc. Natl. Acad. Sci. U. S. A.*, 2025, **122**, e2501323122.

50 S. Crossley, J. Faria, M. Shen and D. E. Resasco, Solid Nanoparticles that Catalyze Biofuel Upgrade Reactions at the Water/Oil Interface, *Science*, 2010, **327**, 68–72.

51 Y. Zhang, M. Zhang and H. Yang, Tuning biphasic catalysis reaction with a pickering emulsion strategy exemplified by selective hydrogenation of benzene, *ChemCatChem*, 2018, **10**, 5224–5230.

52 A. M. B. Rodriguez and B. P. Binks, Catalysis in Pickering emulsions, *Soft Matter*, 2020, **16**, 10221–10243.

53 W. Zhang, L. Fu and H. Yang, Micrometer-scale mixing with pickering emulsions: biphasic reactions without stirring, *ChemSusChem*, 2014, **7**, 391–396.

54 B. Xue, T. Xu, D. Li, J. Xu, Y. Li, F. Wang and J. Zhu, A Pickering emulsion of a bifunctional interface prepared from Pd nanoparticles supported on silicane-modified graphene oxide: an efficient catalyst for water-mediated catalytic hydrogenation, *Catal. Sci. Technol.*, 2020, **10**, 1096–1105.

55 A. M. Prophet, D. Limmer and K. R. Wilson, Surfactant Control of Interfacial Reaction Rates in Aqueous Microdroplets, *Phys. Chem. Chem. Phys.*, 2025, DOI: **10.1039/D5CP01573A**.

56 H. Hao, L. Ruiz Pestana, J. Qian, M. Liu, Q. Xu and T. Head-Gordon, Chemical transformations and transport phenomena at interfaces, *Wiley Interdiscip. Rev. Comput. Mol. Sci*, 2023, **13**, e1639.

57 D. T. Limmer, A. W. Götz, T. H. Bertram and G. M. Nathanson, Molecular Insights into Chemical Reactions at Aqueous Aerosol Interfaces, *Annu. Rev. Phys. Chem.*, 2024, **75**, 111–135.

58 T. Ishiyama, T. Imamura and A. Morita, Theoretical Studies of Structures and Vibrational Sum Frequency Generation Spectra at Aqueous Interfaces, *Chem. Rev.*, 2014, **114**, 8447–8470.

59 D. Ben-Amotz, Interfacial chemical reactivity enhancement, *J. Chem. Phys.*, 2024, **160**(8), 084704.